Compensation Parameter Optimization of Inductive Wireless Power Transfer System for Low Stray Magnetic Field

Yueshi Guan, *Senior Member, IEEE*, Yongkang Qiao, Jianwei Mai, Yijie Wang, *Senior Member, IEEE*, and Dianguo Xu, *Fellow, IEEE*

***Abstract*—During the operation of an unmanned aerial vehicle (UAV) inductive wireless power transfer (IPT) system, stray magnetic fields from the magnetic coupler can compromise the safety of the UAV's electronic equipment. This issue limits the widespread adoption of the parallel coupler, despite its high coupling coefficient. This article proposes an improved design that allows designers achieve a lower magnetic field distribution in a parallel coupler without compromising its transfer power, which offers a balanced approach to optimizing the trade-off between high coupling coefficient and low stray magnetic field distribution in couplers for UAV-IPT. Specifically, the magnetic field generated by the transmitter coil and receiver coil is analytically studied, and an improved compensation parameter design is presented to achieve a lower magnetic field distribution. Besides, it also compares the stray magnetic field distribution characteristics of the improved design described in this article with that of the conventional design widely used for the parallel coupler. Finally, a system is implemented to verify the low stray magnetic field distribution characteristics. The experimental results show that the improved design reduces the stray magnetic field around the UAV's electronic equipment by 40.3% compared to the conventional design, while maintaining the same transfer power.**

***Index Terms*—Compensation parameter design, inductive wireless power transfer (IPT), low stray magnetic field, unmanned aerial vehicle (UAV).**

I. Introduction

THE rise of unmanned aerial vehicle (UAVs) has significantly advanced the development of various industries, such as electric power inspection, agriculture and forestry plant protection, and border patrol [1]. However, the battery endurance capability has been the main factor limiting the widespread adoption of UAVs [2]. Due to the limitation of the battery power density, if the endurance of the battery is improved, larger volume and heavier weight of the UAV's battery is required, which is not friendly to UAVs. To enhance the operational range and duration of UAVs, UAV-inductive wireless power transfer (IPT) systems are emerging as a promising flexible charging solution and have become a research focal point [3], [4].

To reduce the weight and improve the structural rigidity of the UAVs, there is a consensus against using ferrite cores in the receiver of a UAV-IPT system, since ferrites are both heavy and fragile [5], [6], [7]. Besides, high coupling coefficient should be paid more attention for achieving high-power and high-efficiency power transfer when designing the transmitter and the receiver. There have been some researches that focus on the magnetic coupler design for UAV-IPT.

The parallel structure is proposed earlier and widely used because of its simple structure and high coupling coefficient. Arteaga et al. [8] and Aldhaher et al. [9] proposes a parallel structure with a configuration of large-to-small coils, where the UAV's anti-collision frame is replaced with the RX. This parallel structure has a simple structure and is easy to install, but the *RX* on the anti-collision frame causes strong electromagnetic interference to the UAV's electronic equipment. Zhou et al. [10] and Song et al. [11] place the *RX* under the UAV's body for reducing the electromagnetic interference to the UAV's electronic equipment. However, as the EMI study in [12], this parallel structure still causes amount of stray magnetic fields through the UAV's body. Excessive stray magnetic fields typically cause thermal losses in environments with magnetically conductive materials. Ke et al. [13] winds the *RX* at the bottom of the landing gear leg, as shown in Fig. 1(a), to relieve the electromagnetic interference of stray magnetic fields and improve the coupling coefficient. Unfortunately, the adverse effect of stray magnetic fields to camera or other sensors is still inevitable. Although add shielding layers between the magnetic coupler and UAV's electronic devices can effectively reduce stray magnetic fields, this will increase the UAV's load capacity and reduce its mobility.

To mitigate electromagnetic interference in UAV-IPT systems, The work in [14], [15], [16], [17], [18], [19], [20], and [21] proposed adopting the orthogonal structure for its low stray magnetic field distribution characteristics. For example, the orthogonal three-coil coupler shown in Fig. 1(b) typically consists of a bipolar *TX* and multiple *RX*s wound around the

Received 1 December 2024; accepted 5 January 2025. Date of publication 8 January 2025; date of current version 26 February 2025. This work was supported in part by the National Natural Science Foundation of China under Grant 52377175, and in part by the Delta Power Electronics Science and Education Development Program of Delta Group under Grant DREK2023003. Recommended for publication by Associate Editor S. Mekhilef. *(Corresponding author: Yueshi Guan.)*

The authors are with the School of Electrical Engineering and Automation, Harbin Institute of Technology, Harbin 150001, China (e-mail: guanyueshi@hit.edu.cn; yongkangqiao@stu.hit.edu.cn; maijianwei@hit.edu.cn; wangyijie@hit.edu.cn; xudiang@hit.edu.cn).

Color versions of one or more figures in this article are available at https://doi.org/10.1109/TPEL.2025.3527723.

Digital Object Identifier 10.1109/TPEL.2025.3527723

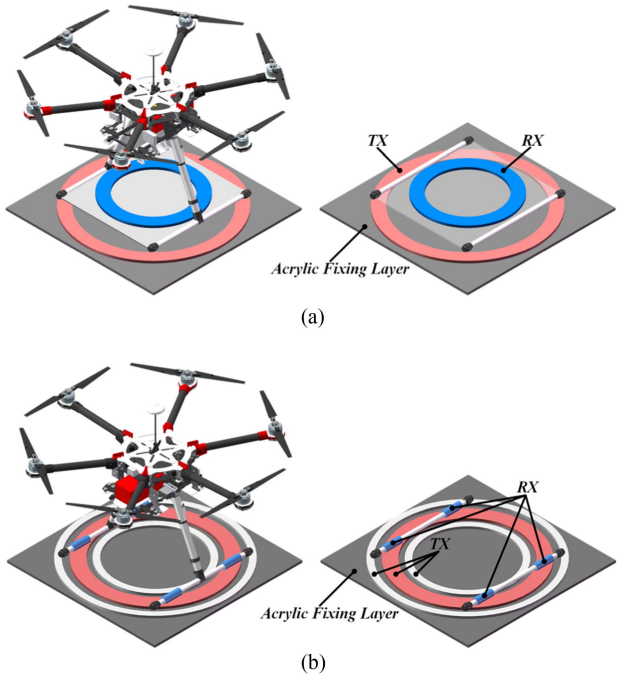

Fig. 1. Magnetic couplers in UAV-IPT systems. (a) Parallel coupler. (b) Orthogonal three-coil coupler.

TABLE I
COMPARISON OF TWO COUPLER STRUCTURES

Coupler type	Coupling coefficient	Stray magnetic field distribution
Parallel Structure	High	High
Orthogonal Structure	Low	Low
This article	**High**	**Low**

landing gear legs. The bipolar structure confines the magnetic field to a limited area, effectively suppressing stray magnetic fields around the UAV's electronic components. However, the low coupling coefficient between the *TX* and *RX* presents a significant challenge for orthogonal couplers, limiting their widespread use in high-power and high-efficiency scenarios.

Based on the above analysis, Table I gives the advantages and disadvantages of the two coupler structures. Analysis of Table I highlights a key challenge in existing research: achieving both high coupling coefficient and low stray magnetic field distribution is a difficult design tradeoff for UAV-IPT couplers.

To optimize the tradeoff between high coupling coefficient and low stray magnetic field distribution in UAV-IPT couplers, this article focuses on the parallel coupler shown in Fig. 1(a) and proposes an improvement to its compensation parameter design to reduce stray magnetic field distribution. By the analysis of magnetic field spatial distribution, the stray magnetic field of the parallel coupler is studied and confirmed to be the coupling magnetic field. By the analysis of magnetic field intensity, the analytical relationship between the coupling magnetic field intensity and induced electromotive force is found. Based on this, an improved design is proposed and demonstrated to achieve a lower stray magnetic field distribution in a parallel coupler without compromising its transfer power, compared to the conventional design widely used for UAV-IPT. Subsequently, the compensation parameter design formulas of the improved design are provided, and the load-independent zero phase angle (ZPA) operation and constant output of the improved system are validated. Additionally, an analysis of the impact of misalignment on the stray magnetic field distribution characteristics is conducted, which revealing that the proposed improvement can still suppress stray magnetic fields around the UAV's electronic equipment in the presence of misalignment between the transmitter and receiver. It also compares the coil losses and transfer efficiencies of the improved design with those of the conventional design. Finally, a wireless charging prototype for UAVs is set up to validate the proposal of improvement.

II. Analysis of Magnetic Field and Proposal of Improvement

A. Analysis of Magnetic Field Spatial Distribution

The composition of the parallel magnetic coupler in a UAV-IPT system is depicted in Fig. 1(a). The parallel coupler consists of a transmitter coil (*TX*) and a receiver coil (*RX*). To clarify and intuitively present the magnetic field distribution of the parallel coupler, this article first analyzes the magnetic field distribution when only the *TX* is excited and when only the *RX* is excited, and then analyzes the magnetic field distribution when both *TX* and *RX* are excited. The magnetic field spatial distribution of the parallel coupler is shown on Fig. 2, where the *RX* is positioned away from *TX* by a gap with a height of H_{Gap}.

When only the *TX* is excited, as shown in Fig. 2(a), the *TX* leakage magnetic field intensity ($\mathbf{H}_{1\sigma}$) is distributed in (-H_{Gap}, H_{Gap}), and the *TX* coupling magnetic field intensity ($\mathbf{H}_{1m}$) is distributed in (-∞, $+\infty$). When only the RX is excited, as shown in Fig. 2(b), the *RX* leakage magnetic field intensity ($\mathbf{H}_{2\sigma}$) is distributed in (0, $2H_{\mathrm{Gap}}$), and the RX coupling magnetic field intensity ($\mathbf{H}_{2m}$) is distributed in (-∞, $+\infty$). It can be concluded that in the parallel coupler, the leakage magnetic field intensity ($\mathbf{H}_{\sigma}$, $\mathbf{H}_{\sigma} = \mathbf{H}_{1\sigma} + \mathbf{H}_{2\sigma}$) is distributed in (-$H_{\mathrm{Gap}}$, $2H_{\mathrm{Gap}}$), while the coupling magnetic field intensity ($\mathbf{H}_{m}$, $\mathbf{H}_{m} = \mathbf{H}_{1m} + \mathbf{H}_{2m}$) is distributed in (-$\infty$, $+\infty$).

In practice, when the UAV is parked on a wireless charging platform for charging, the RX and TX are in contact, which means that H_{Gap} is approximately equal to 0. Therefore, the range of $\mathbf{H}_{\sigma}$ approaches a null set, and the stray magnetic field around the UAV is naturally $\mathbf{H}_{m}$, as shown in Fig. 3(a). It is important to note that, due to the inevitable discrepancy between the actual and ideal situations, $\mathbf{H}_{\sigma}$ is very low but remains present. Given that the contribution of $\mathbf{H}_{\sigma}$ to the stray magnetic field is negligible, $\mathbf{H}_{\sigma}$ is not depicted in Fig. 3(a).

For the majority of parallel couplers, the spatial distribution of $\mathbf{H}_{m}$ is nonuniform. To macroscopically analyze and regulate $\mathbf{H}_{m}$, a postprocessing method is proposed in (1), equating the nonuniform $\mathbf{H}_{m}$ illustrated in Fig. 3(a) with the uniform $\mathbf{H}_{M}$ depicted in Fig. 3(b), based on the conservation of magnetic energy in the coupling magnetic field. In the following study,

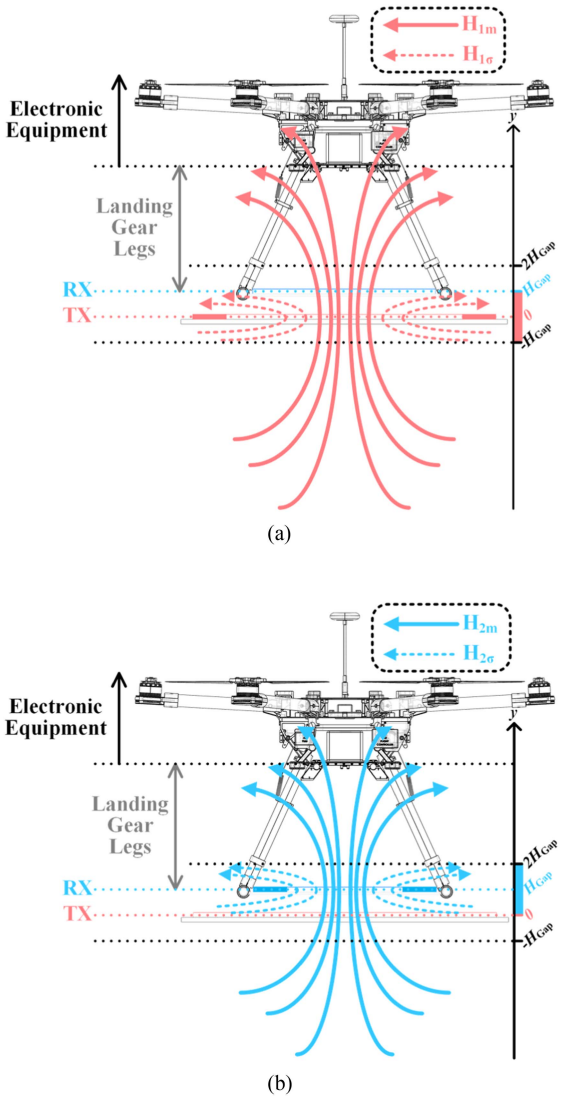

Fig. 2. Magnetic field distribution. (a) When only the *TX* is excited. (b) When only the *RX* is excited.

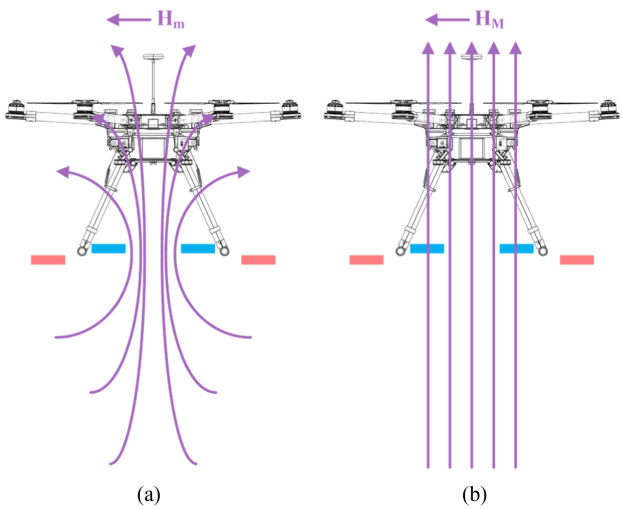

Fig. 3. Magnetic field distribution when *TX* and *RX* are excited. (a) Actual situation. (b) Postprocessing situation.

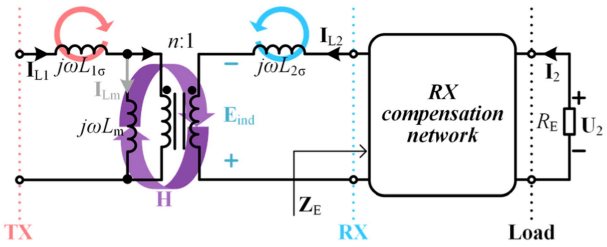

Fig. 4. Equivalent circuit of the parallel coupler.

$\mathbf{H}_M$ will be quantitatively analyzed to assess the stray magnetic field intensity

$$W_m = \int_{V_m} \frac{1}{2}\mu_0 \cdot \mathbf{H}_m^2 \cdot dV = \frac{1}{2}\mu_0 \cdot \mathbf{H}_M^2 \cdot V_m \tag{1}$$

where W_m represents the magnetic energy of the coupling magnetic field; V_m represents the spatial volume of the coupling magnetic field; and μ_0 represents the magnetic permeability.

B. Analysis of Magnetic Field Intensity

The transformer model of the parallel coupler is presented in Fig. 4. $L_{1\sigma}$, $L_{2\sigma}$, and L_m are the *TX* leakage inductance, *RX* leakage inductance, and excitation inductance, respectively. $\mathbf{U}_2$ represents the port voltage of the load. $\mathbf{I}_2$ represents the port current of the load. $\mathbf{U}_2$ is produced by an uncontrolled rectifier, and is in phase with $\mathbf{I}_2$. Hence, a resistance R_E is used to represent the load. $\mathbf{Z}_E$ represents the equivalent impedance from the RX port to the load. $\mathbf{I}_{L1}$ and $\mathbf{I}_{L2}$ represent the port currents of the *TX* and *RX*, respectively. $\boldsymbol{I}_{Lm}$ represents the excitation current (denoted as i_{Lm} in the time domain). $\mathbf{E}_{\text{ind}}$ represents the induced electromotive force in the *RX* loop (denoted as e_{ind} in the time domain).

The relationship between the mutual-inductance model parameters and transformer model parameters is illustrated as follows:

$$\begin{pmatrix} L_{1\sigma} \\ L_{2\sigma} \\ L_m \end{pmatrix} = \begin{pmatrix} 1 & 0 & -n \\ 0 & 1 & -\frac{1}{n} \\ 0 & 0 & n \end{pmatrix} \cdot \begin{pmatrix} L_1 \\ L_2 \\ M \end{pmatrix} \tag{2}$$

$$n = \sqrt{\frac{L_1}{L_2}} \tag{3}$$

where n represents the turns ratio between the *TX* and *RX*.

According to the physical interpretation of the transformer model, $L_{1\sigma}$, $L_{2\sigma}$, and L_m correspond to the *TX* leakage magnetic field, *RX* leakage magnetic field, and coupling magnetic field, respectively. For a parallel coupler, W_m in the active field can be expressed as

$$W_m = \frac{1}{2} L_m i_{Lm}^2. \tag{4}$$

By combining (1) and (4), the value of $\mathbf{H}_M$ (H) can be derived as

$$H = \sqrt{\frac{L_m}{\mu_0 V_m}} \cdot i_{Lm}. \tag{5}$$

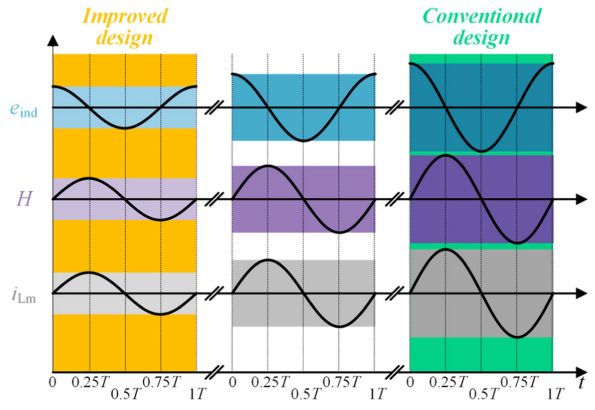

Fig. 5. Relationship between i_{Lm}, H, and e_{ind} in the time domain.

By taking the derivative with respect to time (t) on both sides of (5), the following expression can be obtained:

$$\frac{dH}{dt} = \sqrt{\frac{L_m}{\mu_0 V_m}} \cdot \frac{di_{Lm}}{dt} = \sqrt{\frac{L_m}{\mu_0 V_m}} \cdot \frac{ne_{\text{ind}}}{L_m} = \sqrt{\frac{n}{\mu_0 V_m M}} \cdot e_{\text{ind}}. \tag{6}$$

Applying the Fourier transform to both sides of (6) produces the following result:

$$j\omega \cdot \mathbf{H} = \sqrt{\frac{n}{\mu_0 V_m M}} \cdot \mathbf{E}_{\text{ind}} \tag{7}$$

where $\mathbf{H}$ is the phasor domain representation of H.

Equation (7) represents a differential form of Faraday's law of electromagnetic induction, which states that the induced electromotive force is directly proportional to the rate of change of the coupling magnetic field intensity over time. In the steady state of a UAV-IPT system, as depicted in Fig. 5, H varies sinusoidally in phase with i_{Lm} while remaining orthogonal to e_{ind}. Further analysis indicates that achieving a larger induced electromotive force in the *RX* loop while maintaining a constant cycle time (T) requires an increase in the amplitude of the coupling magnetic field intensity.

In the RX loop, according to Kirchhoff's voltage law, $\mathbf{E}_{\text{ind}}$ can be expressed as

$$\mathbf{E}_{\text{ind}} = \overbrace{\mathbf{I}_{L2} \cdot \text{Re}(\mathbf{Z}_E)}^{\mathbf{U}_{\text{Re}}} + \overbrace{\mathbf{I}_{L2} \cdot j\left[\text{Im}(Z_E) + wL_{2s}\right]}^{\mathbf{U}_{\text{Im}}} \tag{8}$$

where $\mathbf{U}_{\text{Re}}$ and $\mathbf{U}_{Im}$ represent the resistance voltage and reactance voltage in the *RX* loop, respectively, and their sum constitutes $\mathbf{E}_{\text{ind}}$. The operator "Re" (or "Im") represents the real (or imaginary) part of an impedance.

When the receiver is loaded, the induced voltage generates induced current in the *RX* loop. Meanwhile, the active power consumed by R_{E} corresponds to the transfer power (P_t), which is also equal to the active power consumed by Re($\mathbf{Z}_E$) and can be expressed as

$$P_t = \frac{1}{2} \cdot \text{I}_2^2 R_E = \frac{1}{2} \cdot \text{I}_{L2}^2 \text{Re}(\mathbf{Z}_E) \tag{9}$$

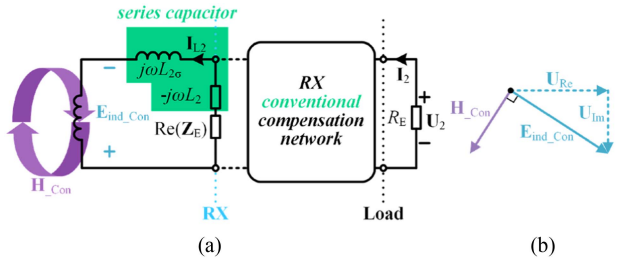

Fig. 6. RX conventional compensation design. (a) Equivalent circuit. (b) Phasor diagram.

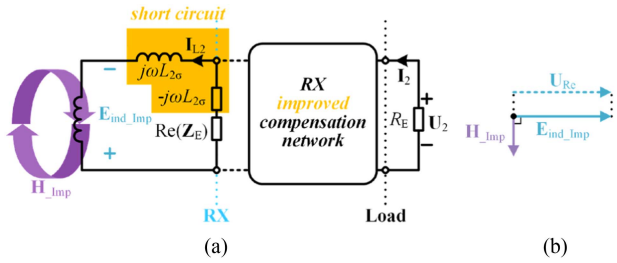

Fig. 7. *RX* improved compensation design. (a) Equivalent circuit. (b) Phasor diagram.

where I_2 and I_{L2} represent the maximum values of $\mathbf{I}_2$ and $\mathbf{I}_{L2}$, respectively.

By combining (7)–(9), the analytical relationship between $\mathbf{H}$ and P_t is derived as follows:

$$\mathbf{H} = \sqrt{\frac{2nP_t}{\mu_0 V_m \omega^2 M}} \cdot \frac{\left[\text{Im}(\mathbf{Z}_E) + \omega L_{2\sigma} - j\text{Re}(\mathbf{Z}_E)\right]}{\sqrt{\text{Re}(\mathbf{Z}_E)}} \cdot e^{j\varphi_{iL2}} \tag{10}$$

where φ_{iL2} represents the phase angle of $\mathbf{I}_{L2}$ (assuming $\varphi_{iL2} = 0$ for subsequent analysis).

C. Proposal of Improvement

In the conventional design widely used for UAV-IPT systems, the *RX* compensation network is configured to ensure that Im($\mathbf{Z}_E$) remains equal to -ωL_2 and is unaffected by variations in R_E. As shown in Fig. 6(a), $j\omega L_{2\sigma}$ and jIm($\mathbf{Z}_E$) are connected in series, which can be represented as a series capacitor.

For the conventional design, the induced electromotive force ($\mathbf{E}_{\text{ind\_Con}}$) can be calculated from (8) and is presented in (11). The coupling magnetic field intensity ($\mathbf{H}_{\text{\_Con}}$) is derived from (10) and detailed in (12). The phasor relationship between $\mathbf{E}_{\text{ind\_Con}}$ and $\mathbf{H}_{\text{\_Con}}$ is illustrated in Fig. 6(b)

$$\mathbf{E}_{\text{ind\_Con}} = \overbrace{\mathbf{I}_{L2} \cdot \text{Re}(\mathbf{Z}_E)}^{\mathbf{U}_{\text{Re}}} + \overbrace{\mathbf{I}_{L2} \cdot \left(-j\frac{\omega M}{n}\right)}^{\mathbf{U}_{\text{Im}}} \tag{11}$$

$$\mathbf{H}_{\text{\_Con}} = \sqrt{\frac{2nP_t}{\mu_0 V_m \omega^2 M}} \cdot \frac{\left[-\frac{\omega M}{n} - j\text{Re}(\mathbf{Z}_E)\right]}{\sqrt{\text{Re}(\mathbf{Z}_E)}}. \tag{12}$$

This article proposes an improved design illustrated in Fig. 7(a), where the *RX* compensation network is structured to

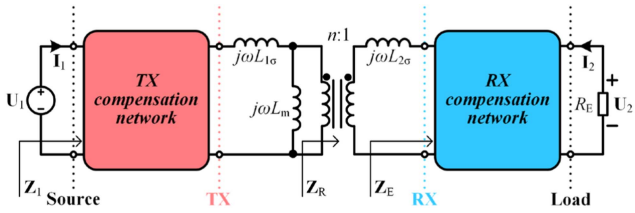

Fig. 8. *TX* compensation network and *RX* compensation network in the system circuit.

ensure that Im($\mathbf{Z}_E$) equals -$\omega L_{2\sigma}$ and is unaffected by changes in R_{E}. Here, $j\omega L_{2\sigma}$ and jIm($\mathbf{Z}_E$) cancel each other out, which can be equivalent to a short circuit.

For the improved design, the induced electromotive force ($\mathbf{E}_{\mathrm{ind\_Imp}}$) can also be calculated from (8) and is presented in (13). The coupling magnetic field intensity ($\mathbf{H}_{\mathrm{\_Imp}}$) is derived from (10) and detailed in (14). The phasor relationship between $\mathbf{E}_{\mathrm{ind\_Imp}}$ and $\mathbf{H}_{\mathrm{\_Imp}}$ is shown in Fig. 7(b)

$$\mathbf{E}_{\mathrm{ind\_Imp}} = \overbrace{\mathbf{I}_{L2}\cdot \mathrm{Re}\left(\mathbf{Z}_E\right)}^{\mathbf{U}_{\mathrm{Re}}} + \overbrace{\mathbf{I}_{L2}\cdot j0}^{\mathbf{U}_{\mathrm{Im}}} \tag{13}$$

$$\mathbf{H}_{\mathrm{\_Imp}} = \sqrt{\frac{2nP_t}{\mu_0 V_m \omega^2 M}}\cdot\frac{-j\mathrm{Re}\left(\mathbf{Z}_E\right)}{\sqrt{\mathrm{Re}\left(\mathbf{Z}_E\right)}}. \tag{14}$$

To ensure the fairness of the analysis, P_t of the improved design is same as that of the conventional design. By comparing (12) and (14), the following conclusion can be drawn:

$$\frac{|\mathbf{H}_{\mathrm{\_Con}}|}{|\mathbf{H}_{\mathrm{\_Imp}}|} = \left|\frac{\frac{\omega M}{n}}{j\mathrm{Re}\left(\mathbf{Z}_E\right)}+1\right| > 1 \Rightarrow |\mathbf{H}_{\mathrm{\_Con}}| > |\mathbf{H}_{\mathrm{\_Imp}}|. \tag{15}$$

Equation (15) indicates that the magnetic field intensity of the improved design is lower than that of the conventional design at an equivalent power level. Comparing Figs. 6(b) and 7(b) reveals that the reduction in stray magnetic fields is attributed to the improved design's ability to eliminate $\mathbf{U}_{\mathrm{Im}}$ and thereby reduce $\mathbf{E}_{\mathrm{ind}}$. As depicted in Fig. 5, a smaller induced electromotive force corresponds to a lower magnetic field intensity.

Consequently, the proposed improvement can help designers achieve a lower stray magnetic field distribution in a parallel coupler without compromising its transfer power, which offers a balanced approach to optimizing the tradeoff between high coupling coefficient and low stray magnetic field distribution in couplers for UAV-IPT.

III. Analysis of Improved System

A. Compensation Parameter Design

As illustrated in Fig. 8, the *TX* compensation network links the source to the *TX* port, while the *RX* compensation network connects the RX port to the load. $\mathbf{U}_1$ represents the port voltage of the source. $\mathbf{I}_1$ represents the port current of the source. $\mathbf{Z}_1$ represents the equivalent impedance from the source to the load. $\mathbf{Z}_R$ represents the reflected impedance of the receiver loop. This article focuses solely on low-order compensation networks, including T-type and S-type configurations, and proposes an improved compensation parameter design for a low stray magnetic field distribution in parallel couplers. If designers aim to employ higher-order compensation networks, they can apply the design principles outlined in this article to derive corresponding compensation parameter designs.

TABLE II
RX Improved Compensation Network

Type	Network structure	Parameter design
T	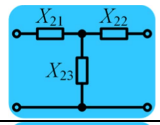	$\begin{cases} X_{22} = -X_{23} \\ X_{21}+X_{23} = -\omega L_{2\sigma} \end{cases}$
S	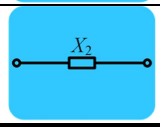	$X_2 = -\omega L_{2\sigma}$

TABLE III
TX Improved Compensation Network

Type	Network structure	Parameter design
T	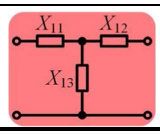	$\begin{cases} X_{12}+X_{13} = -\omega L_{1\sigma} \\ X_{11} = \dfrac{X_{13}^2}{\omega L_{\mathrm{m}}} - X_{13} \end{cases}$

In the improved design, the *RX* compensation network is configured to ensure that the following equation is satisfied to achieve a low stray magnetic field distribution:

$$\begin{cases} \mathrm{Im}\left(\mathbf{Z}_E\right) = -\omega L_{2\sigma} \\ \frac{\partial \mathrm{Im}(\mathbf{Z}_E)}{\partial R_E} = 0 \end{cases}. \tag{16}$$

Based on (16), the compensation parameter design formulas for the T-type and S-type networks are derived, as given in Table II. X_{21}, X_{22}, X_{23}, and X_2 represent the reactance parameters of compensation components in the *RX* compensation network.

In the improved design, the *TX* compensation network is designed to ensure that the following equation is satisfied for the load-independent ZPA operation

$$\begin{cases} \mathrm{Im}\left(\mathbf{Z}_1\right) = 0 \\ \frac{\partial \mathrm{Im}(\mathbf{Z}_1)}{\partial R_E} = 0 \end{cases}. \tag{17}$$

The second equation in (17) can be transformed as follows:

$$\frac{\partial \mathrm{Im}\left(\mathbf{Z}_1\right)}{\partial R_E} = \frac{\partial \mathrm{Im}\left(\mathbf{Z}_1\right)}{\partial \mathbf{Z}_R}\cdot\frac{\partial \mathbf{Z}_R}{\partial R_E} = 0 \overset{\frac{\partial \mathbf{Z}_R}{\partial R_E}\neq 0}{\Rightarrow} \frac{\partial \mathrm{Im}\left(\mathbf{Z}_1\right)}{\partial \mathbf{Z}_E} = 0. \tag{18}$$

Based on (17) and (18), the compensation parameter design formulas for the T-type network are derived, as presented in Table III. X_{11}, X_{12}, and X_{13} represent the reactance parameters of compensation components in the *TX* compensation network. It should be noted that the S-type compensation network cannot ensure that (17) and (18) are satisfied, and then it is not suitable for the *TX* improved compensation network.

Thus, the improved design is completed and illustrated in Fig. 9. Multiple components with the same background color

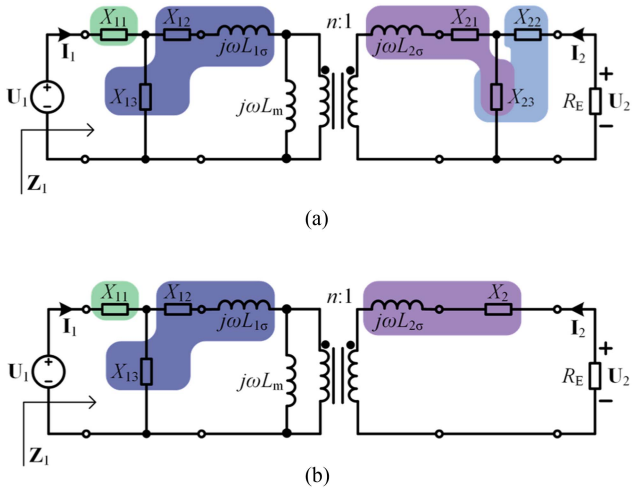

Fig. 9. Improved compensation parameter design. (a) T/T-type. (b) T/S-type.

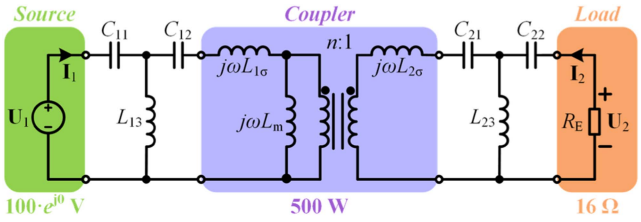

Fig. 10. Circuit of the UAV-IPT system with a CLC/CLC compensation network.

TABLE IV
PARAMETERS OF COUPLER

Symbols	Parameters	Values
M	Mutual inductance	93.16 μH
L_1	TX inductance	130.15 μH
L_2	RX inductance	87.80 μH
ω	Operating angular frequency	2π·85000 rad/s

resonate and neutralize one another. The improved design is applicable to two types of network structures: T/T and T/S. X_{11} is utilized to adjust the input impedance angle $\varphi(\mathbf{Z}_1)$ to 0° for achieving ZPA operation, or to slightly greater than 0° for achieving zero voltage switching (ZVS).

B. ZPA Operation and Constant Output Characteristics

The improved design can be applied to various compensation networks, such as *LCC/LCC, CLC/CLC,* and *LCC/S*. This article takes the UAV-IPT system depicted in Fig. 10 as an example to validate the ZPA operation and constant output characteristics of the improved system. The operation state of this system is as follows: $\mathbf{U}_1 = 100{\cdot}e^{j0}$ V; $P_t = 500$ W; and $R_E = 16\ \Omega$. The parameters of coupler and the compensation parameters of the improved design are presented in Tables IV and V, respectively.

For the UAV-IPT system illustrated in Fig. 10, the voltage gain (G_v) is defined as (19), and the transconductance (G_g) is

TABLE V
COMPENSATION PARAMETERS OF IMPROVED DESIGN

TX compensation network	RX compensation network
$C_{11} = 128.59$ nF	$C_{22} = 93.64$ nF
$C_{12} = 56.26$ nF	$C_{21} = 71.95$ nF
$L_{13} = 45.58\ \mu$H	$L_{23} = 37.44\ \mu$H

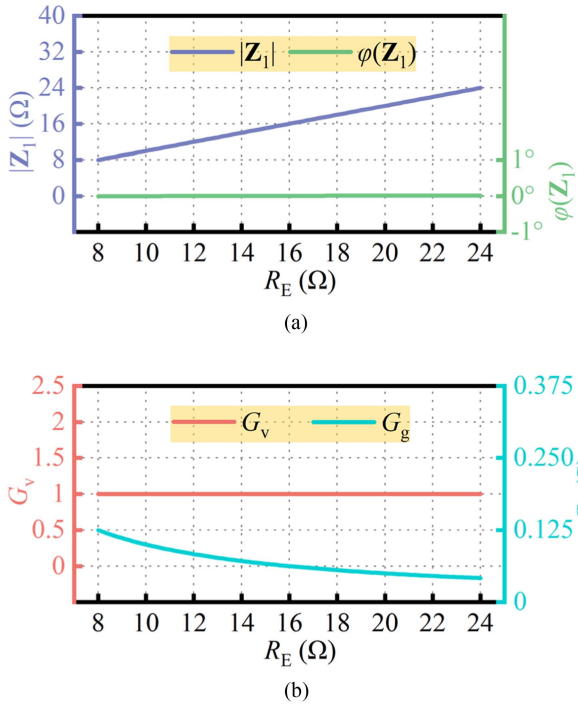

Fig. 11. Variation curves with R_E. (a) $\mathbf{Z}_{\rm in}$. (b) G_v and G_g.

defined as

$$G_v = \frac{|\mathbf{U}_2|}{|\mathbf{U}_1|} = \frac{nL_{23}}{L_{13}} \tag{19}$$

$$G_g = \frac{|\mathbf{I}_2|}{|\mathbf{U}_1|} = \frac{nL_{23}}{R_E L_{13}}. \tag{20}$$

The variation curves of $\mathbf{Z}_1$, G_v and G_g with R_E are depicted in Fig. 11. Analyzing Fig. 11(a) shows that $\varphi(\mathbf{Z}_1)$ barely changes with R_E, which indicates that the improved system can achieve a load-independent ZPA operation. Furthermore, analysis of Fig. 11(b) reveals that G_v hardly varies with R_E while G_g is directly proportional to R_E, which suggests that the improved system with a T/T-type compensation network can achieve a load-independent constant voltage (CV) output. It is worth noting that the improved system with a T/S-type compensation network can achieve a load-independent constant current (CC) output, as can be determined through circuit analysis.

C. Stray Magnetic Field Distribution Characteristics

As illustrated in Fig. 12(a), during a UAV-IPT system working, stray magnetic fields can interfere with the operation of the UAV's electronic equipment. In order to simplify the analysis process, this article only considers the stray

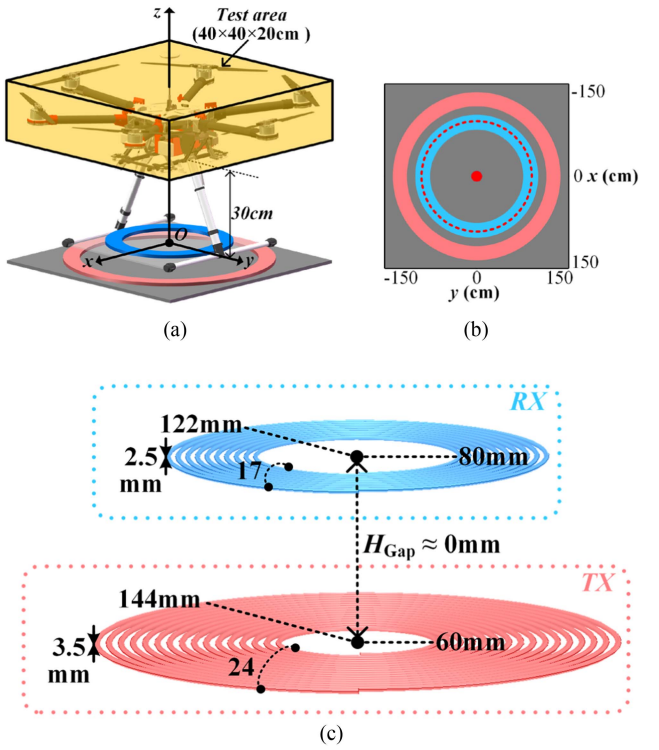

Fig. 12. Analysis of stray magnetic field distribution characteristics. (a) Test area. (b) Top view of coupler in the absence of misalignment. (c) Diagram of coupler.

magnetic field around the UAV's electronic equipment, i.e., within the designated test area. The parallel coupler shown in Fig. 12(c) is selected as the subject of analysis and its top view is presented in Fig. 12(b). The analysis is performed using the circuit depicted in Fig. 10, maintaining identical source, load, and transfer power between the improved and conventional designs.

If a UAV undergoes a typical radial misalignment, the receiver and the landing position described in Fig. 12(a) will be separated by a distance (denoted as y), as shown in Fig. 13. When $y = 0$ mm, there is no misalignment between the transmitter and receiver. When $y = 20$ mm, the receiver is about to exit the area covered by the transmitter. By finite element simulation, the stray magnetic field distribution characteristics within the range of $0 \leq y \leq 20$ mm is obtained and shown in Fig. 13.

Analyzing Fig. 13 shows that the stray magnetic field intensity of the improved design is consistently lower than that of the conventional design within the range of $0 \leq y \leq 20$ mm. When the receiver is misaligned along the y-axis, the transfer power of the UAV-IPT system shows a downward trend and the reduction rate of the stray magnetic field intensity also gradually decreases. Specifically, with a misalignment of 20 mm along the Y-axis, the improved design can reduce the stray magnetic field intensity by 40.4%. Based on these characteristics, it is evident that using the improved design can still suppress stray magnetic fields around the UAV's electronic equipment in the presence of misalignment between the transmitter and receiver.

TABLE VI
EXPERIMENTAL PLATFORM CONFIGURATION

Parameters	Part numbers or Values
DC input voltage (V_{in})	60 – 100 V
Operating frequency (f_o)	85 kHz
Self-resonant frequency (f_c)	85 kHz
Load resistance (R_L)	10 – 30 Ω
Inverter MOSFETs (Q_1-Q_4)	IRF300P226
Rectifier diodes (D_1-D_4)	SBR40U300CT

TABLE VII
PARAMETERS OF MAGNETIC COUPLER

Parameters	Part numbers or Values
Coil type of *TX*	Planar spiral structure
Internal radius of *TX* (R_{int1})	60 mm
External radius of *TX* (R_{ext1})	142 mm
Wire diameter of *TX* (D_{wire1})	3.43 mm
Wire length of *TX* (L_{wire1})	15.21 m
Turns number of *TX* (N_1)	24
Wire type of *TX*	0.1 mm diameter, 600-strand Litz wire
Quality Factor of *TX* at f_c (Q_{L1})	139.07
Gap height (H_{Gap})	about 0mm
Coil type of *RX*	Planar spiral structure
Internal radius of *RX* (R_{int2})	80 mm
External radius of *RX* (R_{ext2})	124.54 mm
Wire diameter of *RX* (D_{wire2})	2.62 mm
Wire length of *RX* (L_{wire2})	10.91 m
Turns number of *RX* (N_2)	17
Wire type of *RX*	0.1 mm diameter, 350-strand Litz wire
Quality Factor of *RX* at f_c (Q_{L2})	252.30

TABLE VIII
COMPENSATION PARAMETERS CONFIGURATION

Conventional design		Improved design	
TX	*RX*	*TX*	*RX*
$C_{11} = 48.84$ nF	$C_{22} = 93.64$ nF	$C_{11} = 128.59$ nF	$C_{22} = 93.64$ nF
$C_{12} = 17.35$ nF	$C_{21} = 27.97$ nF	$C_{12} = 56.24$ nF	$C_{21} = 71.91$ nF
$L_{13} = 71.77$ μH	$L_{23} = 37.44$ μH	$L_{13} = 45.57$ μH	$L_{23} = 37.44$ μH

IV. EXPERIMENTAL VERIFICATION

A. Experimental Setup

To verify the performance of the improved design, an experimental platform for UAV wireless charging was constructed, as shown in Fig. 14. During the experiments, the compensation network structure, source, load, and transfer power in the proposed design are kept identical to those in the conventional design. The configuration of the experimental platform is given in Table VI. The experimental platform's magnetic coupler consists of two planar spiral coils, detailed in Fig. 15. The size and inductance parameters of the magnetic coupler are given in Table VII. The *CLC/CLC* compensation network parameters of two different designs are given in Table VIII.

The preceding analysis indicates that in the absence of misalignment between the transmitter and receiver, the system's power transfer capability is at its peak, and the interference from stray magnetic fields affecting UAVs is also most pronounced. Therefore, in the experimental analysis below, only the system operating conditions without misalignment are experimentally studied.

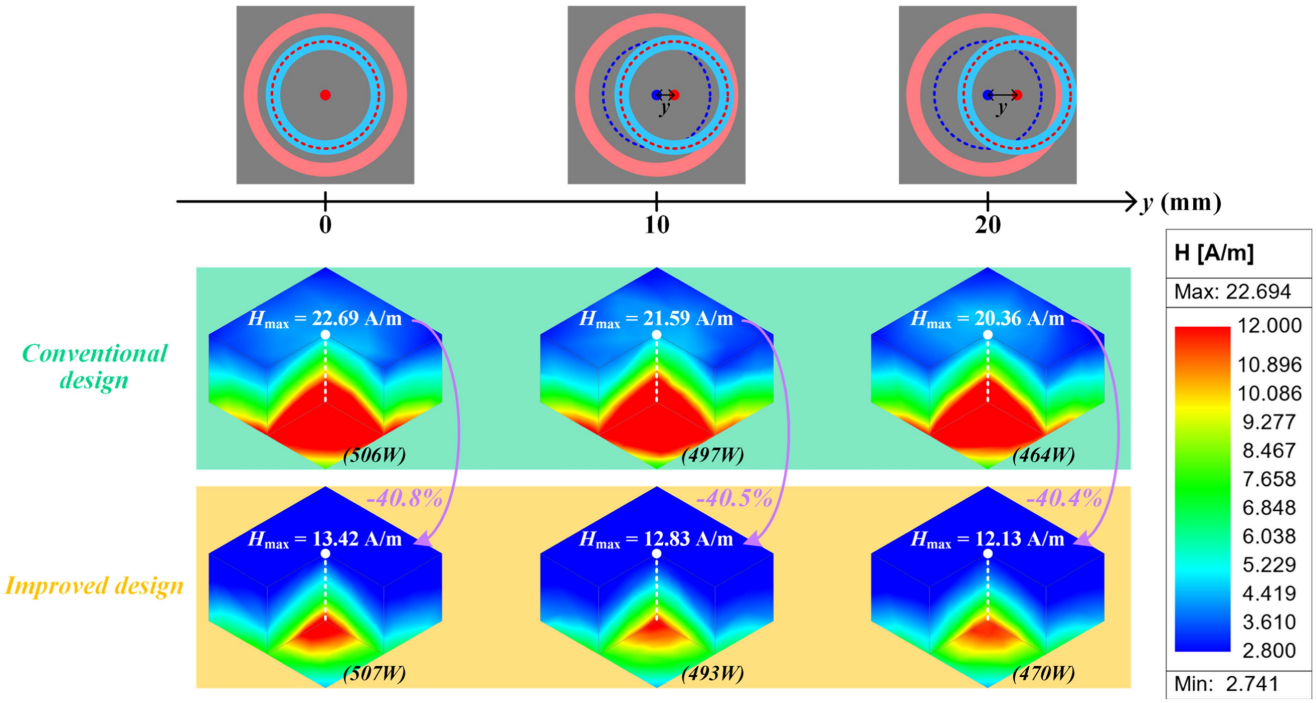

Fig. 13. Stray magnetic field distribution characteristics.

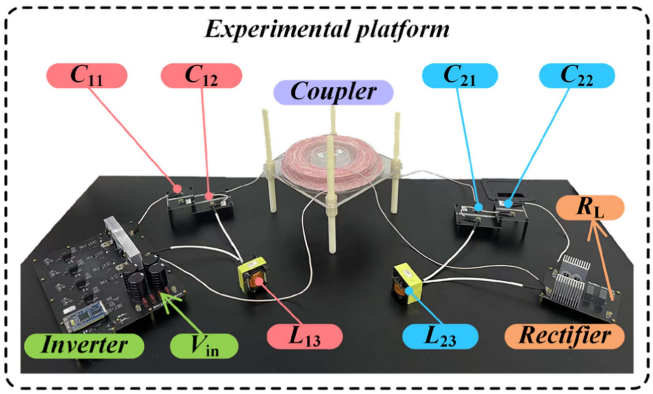

Fig. 14. Experimental platform.

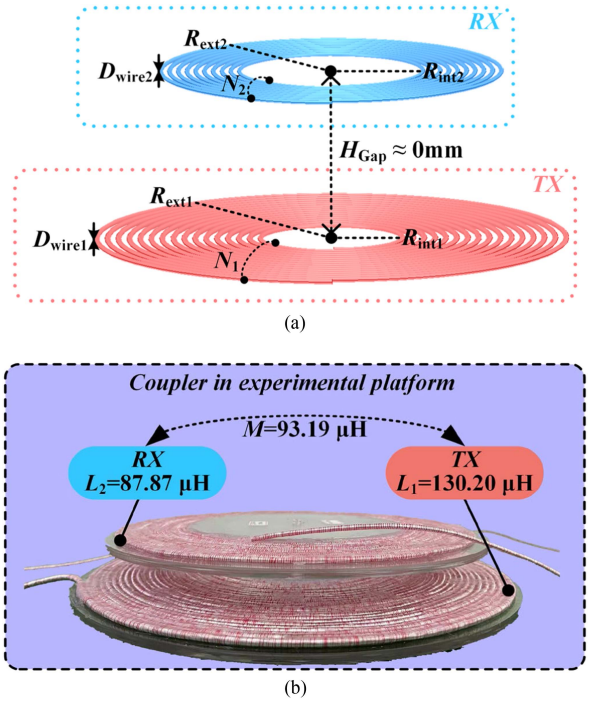

Fig. 15. Magnetic coupler in the experimental platform. (a) Size parameters. (b) Inductance parameters.

B. Results and Analysis

The key waveforms of the improved design under certain load resistances are displayed in Fig. 16(a) and (b). The depicted signals include: u_1 is the port voltage of the source; u_2 is the port voltage of the load; and i_1 is the port current of the source. By calculating the amplitude ratio and phase difference of this signals, the following values can be obtained: input impedance $\varphi(\mathbf{Z}_1) \approx 0°$, voltage gain $G_v \approx 1$. Similarly, the variation curves of $\varphi(\mathbf{Z}_1)$, G_v are presented as Fig. 17(a). Analysis of Fig. 17(a) shows that $\varphi(\mathbf{Z}_1)$ and G_v barely changes within the range of $10\,\Omega \leq R_L \leq 30\,\Omega$, which indicates that using the improved *CLC/CLC* compensation network can achieve a load-independent ZPA operation and CV output.

The transfer power (P_t) and efficiency (denoted as η_t) from the source to the load can be measured with a power analyzer. During the process of increasing voltage, the variation curves of η_t with the dc input voltage V_{in} are presented in Fig. 17(b), while P_t of the improved design consistently remains equal to that of the conventional design. Fig. 17(b) illustrates that η_t of the improved design is nearly identical to that of the conventional

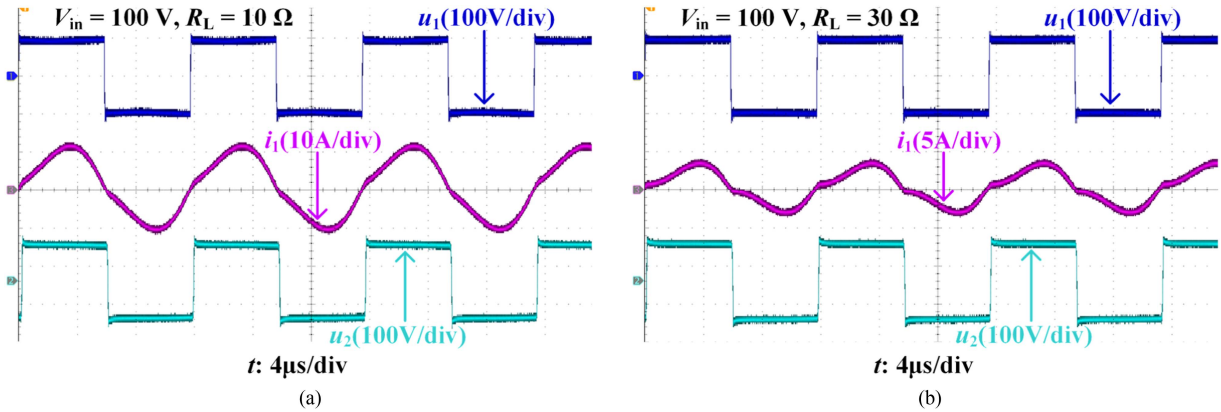

Fig. 16. Experimental waveforms. (a) $R_L = 10\ \Omega$. (b) $R_L = 30\ \Omega$.

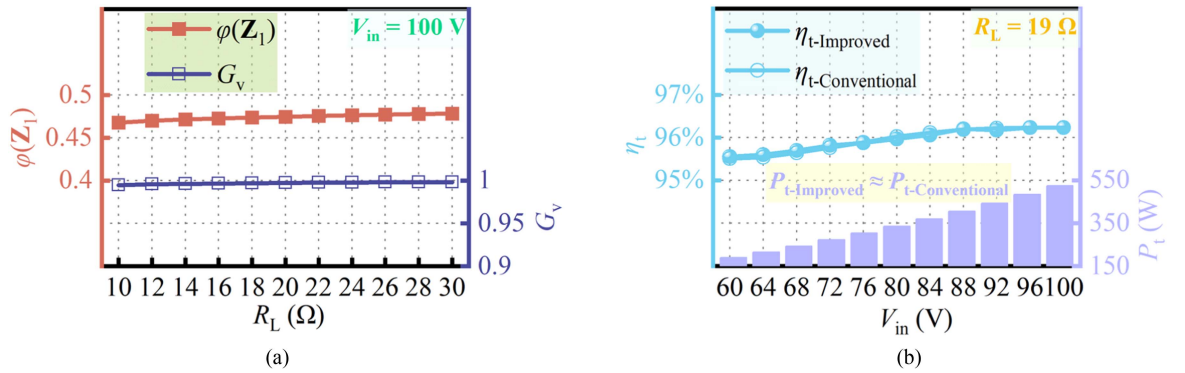

Fig. 17. Variation curves. (a) $\varphi(\mathbf{Z}_1)$ and G_v. (b) P_t and η_t.

design. Specifically, when the dc input voltage is 100 V, the improved design achieves a transfer power of 523W with an efficiency of 96.2%.

The RX is located on the x–y plane at $z = 0$, as shown in Fig. 18. To verify the low stray magnetic field characteristics of the improved design, using a EHP-200A magnetic field measuring instrument with a 92 × 92 × 109 mm sensor to measure the x-y plane at $z = 30$ cm, $z = 40$ cm, and $z = 50$ cm, respectively. When the transfer power of the improved design equals that of the conventional design, the magnetic field intensity is measured using the EHP200-TS at (0, 0, 30 cm), as shown in Fig. 19(a), (b), and (c), along with the corresponding testing conditions. The stray magnetic field intensity distribution on the $z = 30$ cm, $z = 40$ cm, and $z = 50$ cm planes are shown in Fig. 20(a), (b), (c), (d), (e), and (f).

According to the measured results, the peak values of the stray magnetic field caused by wireless charging all appear at the spatial center position of $x = 0$, $y = 0$. Further, at a spatial position 30 cm away from the *RX*, using the improved design described in this article can reduce the stray magnetic field by 40.3%, compared with the conventional design. Moreover, as the distance between the measurement position and *RX* gradually increases, the reduction rate of the stray magnetic field intensity also gradually decreases.

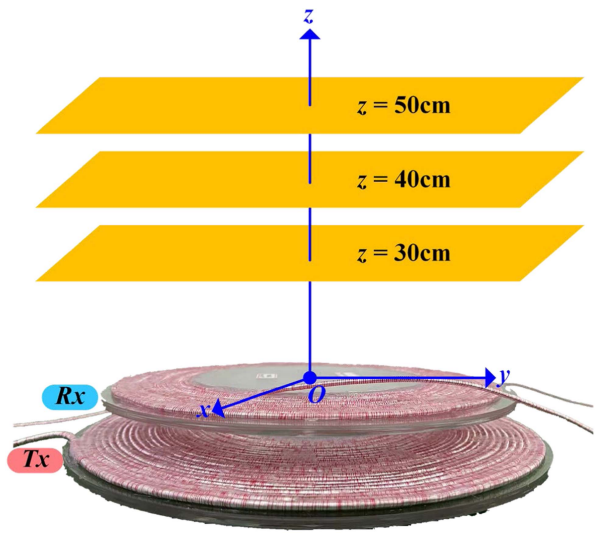

Fig. 18. Stray magnetic field test.

C. Discussion

To demonstrate the superiority of the proposed design, we compare its performance with other techniques, as given in

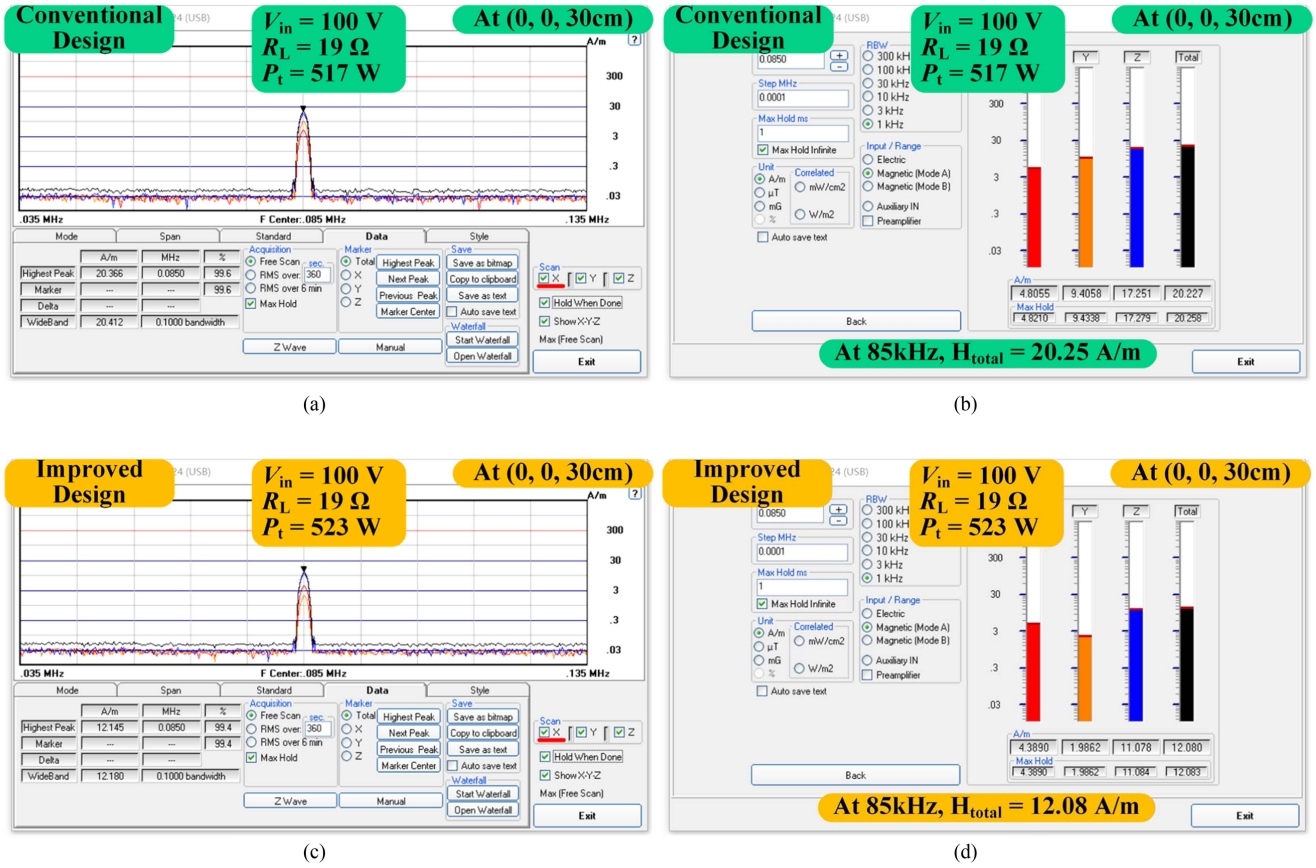

Fig. 19. Test results of stray magnetic field at (0, 0, 30cm). (a) Spectrum of conventional design. (b) Magnetic field intensity of conventional design at 85 kHz. (c) Spectrum of improved design. (d) Magnetic field intensity of improved design at 85 kHz.

TABLE IX
COMPARISON WITH EXISTING WORKS

Coupler type	Citation	Coupling coefficient	Relative position between TX and RX	Transfer power	Transfer efficiency	Stray magnetic field
Orthogonal structure	Wu et al. [14]	0.29	In contact	87 W	84.8%	z=6.2 cm/0.96 μT
	Cai et al. [15]	0.30	In contact	500 W	90.8%	z=10 cm/29 μT
	Huang et al. [17]	0.17	In contact	380 W	87.5%	z=50 cm/1.02 μT
Parallel structure	Campi et al. [12]	0.14	A 100mm air gap	68.7 W	91%	z=10 cm/96 μT
	Wang et al. [22]	0.11	A 54mm air gap	150 W	80.6%	z=50 cm/12 μT
	This article	0.87	In contact	523 W	96.23%	z=50 cm/4.17 μT

Table IX. Two anomalies in Table IX warrant attention: first, the coupler in [14] operates at significantly lower transfer power compared to other references, accounting for its notably low stray magnetic field intensity; second, in [12] and [22], *TX* and RX lack physical contact, unlike in other references, which explains the absence of significant coupling coefficient advantages for these couplers.

Compared to the orthogonal structures in [14], [15], and [17], the proposed design achieves a coupling coefficient increase of at least 190% (relative to [17]), underscoring its ability to retain the parallel structure's high coupling coefficient. This improvement allows the UAV-IPT system to deliver high-power and high-efficiency energy transfer. In comparison to the parallel structures in [12] and [22], the proposed design reduces the stray magnetic field in the coupler by at least 65% (relative to [22]) while maintaining power transfer capability. The comparison further underscores the contribution of this article. This article proposes an improved design that achieves lower magnetic

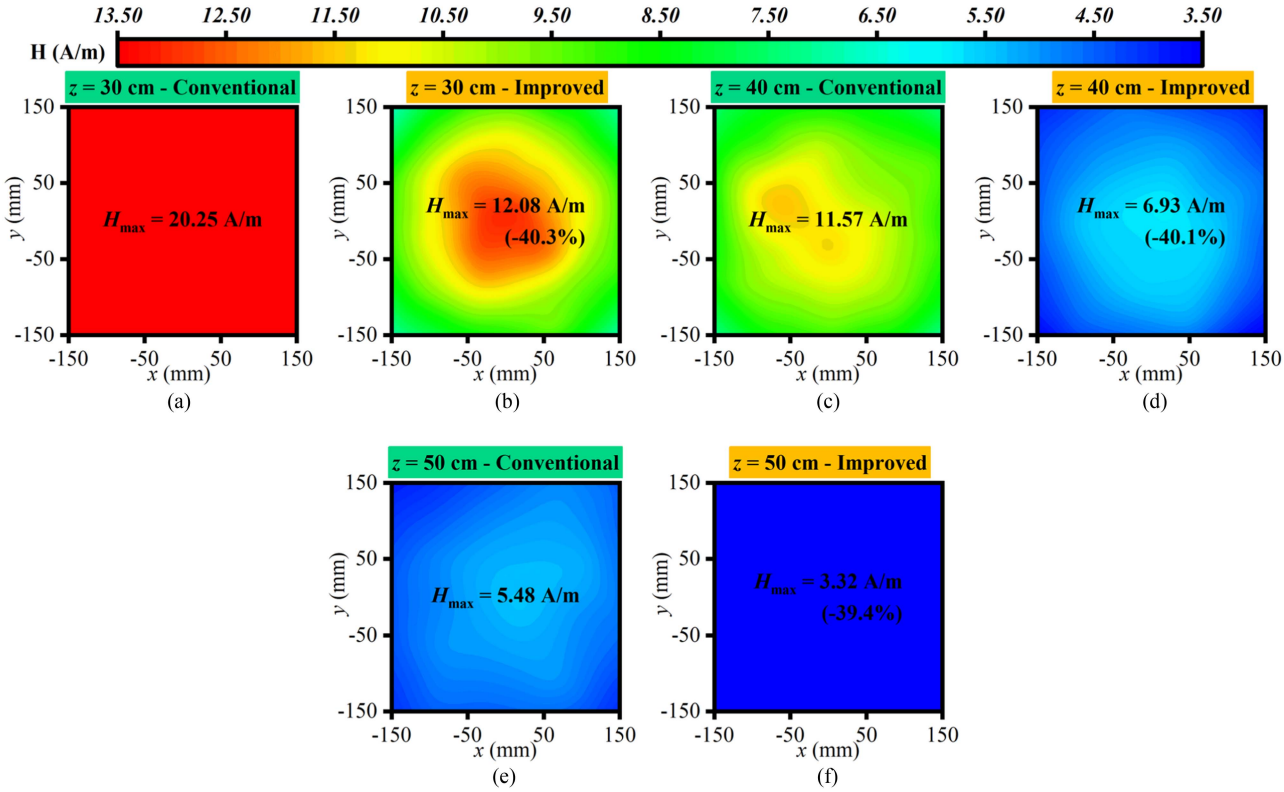

Fig. 20. Stray magnetic field distribution on the test planes. (a) $z = 30$ cm-conventional. (b) $z = 30$ cm-improved. (c) $z = 40$ cm-conventional. (d) $z = 40$ cm-improved. (e) $z = 50$ cm-conventional. (f) $z = 50$ cm-improved.

field distribution in a parallel coupler without compromising power transfer, which offers a balanced approach to optimizing the tradeoff between high coupling coefficient and low stray magnetic field distribution in couplers for UAV-IPT.

While this article lays the groundwork for understanding the spatial distribution and quantitative analysis of stray magnetic fields in parallel couplers for UAV-IPT, several avenues for future exploration remain. For example, extending the proposed design to other near-field IPT applications could unlock new possibilities and expand the scope of this research. Additionally, addressing the current limitation of suppressing stray magnetic fields at a single frequency by employing higher order compensation networks could enhance system performance. Finally, to further validate the findings presented in this article, we recommend conducting additional experiments with T/S-type compensation network structures, such as *LCC/S, LCL/S,* and *CLC/S* networks.

V. Conclusion

In the conventional design widely used for UAV-IPT systems, the *RX* compensation network is usually configured to ensure that the *RX* self-inductance is precisely canceled out to zero for a load-independent ZPA operation and constant output. However, this approach is proven to be ineffective in achieving a low stray magnetic field distribution by the quantitative analysis and experimental results presented in this article. This article proposes an improvement to the compensation parameter design for a lower stray magnetic field distribution. Following the proposed improvement, designers can achieve a lower magnetic field distribution in a parallel coupler without compromising its transfer power. This offers a balanced approach to optimizing the trade-off between high coupling coefficient and low stray magnetic field distribution in couplers for UAV-IPT. Compared to the conventional design, the improved design presented in this article reduces the stray magnetic field around the UAV's electronic equipment by 40.3%, while maintaining the same transfer power. Although, this article uses the *CLC/CLC* compensation network as an example, but the proposed improvement is applicable to other network structures as well. The effectiveness of the improved design is validated through simulation and an experimental prototype.

References

[1] N. Kumar, D. Puthal, T. Theocharides, and S. P. Mohanty, "Unmanned aerial vehicles in consumer applications: New applications in current and future smart environments," *IEEE Consum. Electron. Mag.*, vol. 8, no. 3, pp. 66–67, May 2019.

[2] H. Zhang, Y. Chen, C.-H. Jo, S.-J. Park, and D.-H. Kim, "DC-link and switched capacitor control for varying coupling conditions in inductive power transfer system for unmanned aerial vehicles," *IEEE Trans. Power Electron.*, vol. 36, no. 5, pp. 5108–5120, May 2021.

[3] P. K. Chittoor, B. Chokkalingam, and L. Mihet-Popa, "A review on UAV wireless charging: Fundamentals, applications, charging techniques and standards," *IEEE Access*, vol. 9, pp. 69235–69266, 2021.

[4] Y. Hu, X. Yuan, G. Zhang, and A. Schmeink, "Sustainable wireless sensor networks with UAV-enabled wireless power transfer," *IEEE Trans. Veh. Technol.*, vol. 70, no. 8, pp. 8050–8064, Aug. 2021.

[5] A. B. Junaid, Y. Lee, and Y. Kim, "Design and implementation of autonomous wireless charging station for rotary-wing UAVs," *Aerosp. Sci. Technol.*, vol. 54, pp. 253–266, Jul. 2016.

[6] T. Campi, S. Cruciani, M. Feliziani, and F. Maradei, "High efficiency and lightweight wireless charging system for drone batteries," in *Proc. AEIT Int. Annu. Conf.*, 2017, pp. 1–6.
[7] K. Sang-Won, C. In-Kui, and H. Sung-Yong, "Comparison of charging region differences according to receiver structure in drone wireless charging system," in *Proc. Int. Conf. Inf. Commun. Technol. Convergence*, 2017, pp. 1058–1060.
[8] J. M. Arteaga, S. Aldhaher, G. Kkelis, C. Kwan, D. C. Yates, and P. D. Mitcheson, "Dynamic capabilities of multi-MHz inductive power transfer systems demonstrated with batteryless drones," *IEEE Trans. Power Electron.*, vol. 34, no. 6, pp. 5093–5104, Jun. 2019.
[9] S. Aldhaher, P. D. Mitcheson, J. M. Arteaga, G. Kkelis, and D. C. Yates, "Light-weight wireless power transfer for mid-air charging of drones," in *Proc. 11th Eur. Conf. Antennas Propag.*, 2017, pp. 336–340.
[10] J. Zhou, B. Zhang, W. Xiao, D. Qiu, and Y. Chen, "Nonlinear parity-time-symmetric model for constant efficiency wireless power transfer: Application to a drone-in-flight wireless charging platform," *IEEE Trans. Ind. Electron.*, vol. 66, no. 5, pp. 4097–4107, May 2019.
[11] K. Song, P. Zhang, Z. Chen, G. Yang, J. Jiang, and C. Zhu, "A high-efficiency wireless power transfer system for unmanned aerial vehicle considering carbon fiber body," in *Proc. 22nd Eur. Conf. Power Electron. Appl.*, 2020, pp. 1–7.
[12] T. Campi, F. Dionisi, S. Cruciani, V. De Santis, M. Feliziani, and F. Maradei, "Magnetic field levels in drones equipped with wireless power transfer technology," in *Proc. Asia-Pac. Int. Symp. Electromagn. Compat.*, 2016, pp. 544–547.
[13] D. Ke, C. Liu, C. Jiang, and F. Zhao, "Design of an effective wireless air charging system for electric unmanned aerial vehicles," in *Proc. 43rd Annu. Conf. IEEE-Ind.-Electron.-Soc.*, 2017, pp. 6949–6954.
[14] S. Wu, C. Cai, L. Jiang, J. Li, and S. Yang, "Unmanned aerial vehicle wireless charging system with orthogonal magnetic structure and position correction aid device," *IEEE Trans. Power Electron.*, vol. 36, no. 7, pp. 7564–7575, Jul. 2021.
[15] C. Cai, S. Wu, L. Jiang, Z. Zhang, and S. Yang, "A 500-W wireless charging system with lightweight pick-up for unmanned aerial vehicles," *IEEE Trans. Power Electron.*, vol. 35, no. 8, pp. 7721–7724, Aug. 2020.
[16] S. Wu, C. Cai, X. Liu, W. Chai, and S. Yang, "Compact and free-positioning omnidirectional wireless power transfer system for unmanned aerial vehicle charging applications," *IEEE Trans. Power Electron.*, vol. 37, no. 8, pp. 8790–8794, Aug. 2022.
[17] W. Huang, Y. Zhang, F. Gao, and Y. Yang, "Magnetic structure design of wireless power transfer for free-rotating UAV with low stray magnetic fields," *IEEE Trans. Ind. Electron.*, vol. 72, no. 1, pp. 481–491, Jan. 2025.
[18] C. Cai, D. Shen, S. Wu, X. Liu, and W. Chai, "A high misalignment tolerance IPT system for unmanned aerial vehicles based on multi-winding combined coupling," *IEEE Trans. Transp. Electrific.*, vol. 10, no. 4, pp. 8566–8574, Dec. 2024.
[19] H. Xu, Z. Huang, X. L. Li, and C. K. Tse, "Misalignment-tolerant IPT coupler with enhanced magnetic flux variation suppression and reduced copper usage," *IEEE Trans. Power Electron.*, vol. 39, no. 8, pp. 10506–10517, Aug. 2024, doi: 10.1109/TPEL.2024.3384754.
[20] C. Zhang et al., "A strong misalignment-tolerance wireless power transfer system based on dynamic diffusion magnetic field for unmanned aerial vehicle applications," *IEEE Trans. Power Electron.*, vol. 39, no. 11, pp. 14129–14134, Nov. 2024.
[21] H. Xu and Z. Huang, "Alternately arranged segmented transmitter pads with magnetic field complementation for suppressing power fluctuation in dynamic wireless power transfer," *IEEE Trans. Power Electron.*, vol. 39, no. 10, pp. 14091–14102, Oct. 2024.
[22] J. Wang, R. Chen, C. Cai, J. Zhang, and C. Wang, "An onboard magnetic integration-based WPT system for UAV misalignment-tolerant charging with constant current output," *IEEE Trans. Transp. Electrific.*, vol. 9, no. 1, pp. 1973–1984, Mar. 2023.

Yueshi Guan (Senior Member, IEEE) was born in Heilongjiang Province, China, in 1990. He received the B.S., M.S., and Ph.D. degrees in electrical engineering from Harbin Institute of Technology (HIT), Harbin, China, in 2013, 2015, and 2019, respectively.

Since 2024, he has been a Professor with the Department of Electrical and Electronics Engineering, HIT. His research interests are in the areas of high frequency and very high frequency converters, single-stage ac/dc converter, and high conversion ratio converters.

Yongkang Qiao was born in Hubei Province, China, in 1998. He received the B.S. and M.S. degrees in electrical engineering in 2020 and 2022, respectively, from Harbin Institute of Technology, Harbin, China, where he is currently working toward the Ph.D. degree in electrical engineering.

His research interests include wireless power transfer and power electronics for unmanned aerial vehicles.

Jianwei Mai was born in Henan, China, in 1994. He received the B.S. and Ph.D. degree in electrical engineering from Harbin Institute of Technology, China, in 2017 and 2022, respectively.

From 2023 to 2024, he was an Assistant Researcher with the Department of Electrical and Electronics Engineering, Harbin Institute of Technology, where he has been an Assistant Professor since 2024. His research interests include inductive power transfer, magnetic coupling structure design and simultaneous wireless power and data transfer.

Yijie Wang (Senior Member, IEEE) was born in Heilongjiang Province, China, in 1982. He received the B.S., M.S., and Ph.D. degrees in electrical engineering from the Harbin Institute of Technology, Harbin, China, in 2005, 2007, and 2012, respectively.

From 2012 to 2014, he was a Lecturer with the Department of Electrical and Electronics Engineering, Harbin Institute of Technology. From 2014 to 2017, he was an Associate Professor. Since 2017, he has been a Professor with the Department of Electrical and Electronics Engineering, Harbin Institute of Technology. His research interests include WPT, dc–dc converters, soft-switching power converters, power factor correction circuits, digital control electronic ballasts, and LED lighting systems.

Dr. Wang is an Associate Editor for IEEE TRANSACTIONS ON INDUSTRIAL ELECTRONICS, IEEE JOURNAL OF EMERGING AND SELECTED TOPICS IN POWER ELECTRONICS, IEEE ACCESS, *IET Power Electronics*, and *Journal of Power Electronics.*

Dianguo Xu (Fellow, IEEE) was born in Heilongjiang, China, in 1960. He received the B.S. degree in control engineering from Harbin Engineering University, Harbin, China, in 1982, and the M.S. and Ph.D. degrees in electrical engineering from the Harbin Institute of Technology (HIT), Harbin, China, in 1984 and 1989, respectively.

In 1984, he joined the Department of Electrical Engineering, HIT, as an Assistant Professor. Since 1994, he has been a Professor with the Department of Electrical Engineering, HIT. From 2000 to 2010, he was the Dean of School of Electrical Engineering and Automation, HIT. He is also the Vice President of HIT. He has authored or coauthored more than 600 technical papers. His research interests include renewable energy generation technology, power quality mitigation, sensorless vector controlled motor drives, and high performance servo system.

Dr. Xu is an Associate Editor for IEEE TRANSACTIONS ON INDUSTRIAL ELECTRONICS, IEEE TRANSACTIONS ON POWER ELECTRONICS, and IEEE JOURNAL OF EMERGING AND SELECTED TOPICS IN POWER ELECTRONICS. He is the Chairman of IEEE Harbin Section. He was the recipient of the 2018 IEEE IAS Outstanding Achievement Award.